Inverse Analysis for the Recovery of Forces Applied to Photoelastic Tactile Transducers

R. E. Saad, A. Bonen, and K. C. Smith
Department of Electrical and Computer Engineering
Computer Integrated Manufacturing Laboratory
University of Toronto
Toronto, Ontario, Canada M5S 3G8

B. Benhabib*
Department of Mechanical and Industrial Engineering
Computer Integrated Manufacturing Laboratory
University of Toronto
Toronto, Ontario, Canada M5S 3G8
e-mail: beno@mie.utoronto.ca

Received August 15, 1996; accepted December 17, 1997

In this paper, the forward and inverse analyses of one- and two-layer photoelastic tactile transducers are presented. For such transducers, an applied force profile generates stresses in the photoelastic layer, making it birefringent. Consequently, circularly polarized light input to the transducer becomes elliptically polarized at the output because of the introduction of a phase-lead distribution. Herein, the forward and inverse analyses of a one-layer photoelastic tactile transducer, under ideal conditions, are first presented. The transducer is modeled using closed form equations based on the theories of elasticity and photoelasticity, which allow the calculation of the light intensity distribution corresponding to an applied force profile. However, to recover the force profile from a light intensity distribution (i.e., the inverse problem), the phase-lead distribution must be determined first. A novel technique is described for this purpose. In the second part of the paper, we consider the forward and inverse analyses of a two-layer transducer, under nonideal conditions, where the light-intensity distribution is no longer noise-free. In the forward analysis, the calculation of

* To whom all correspondence should be addressed.

Journal of Robotic Systems 15(5), 259–280 (1998)

CCC 0741-2223/98/050259-22

the stress distribution in the transducer is implemented by finite-element analysis. The recovery of the phase-lead distribution under noisy conditions, however, constitutes an ill-posed inverse problem. A novel algorithm that accurately and effectively determines the phase-lead distribution from a noisy light-intensity distribution is presented.

1. INTRODUCTION

Photoelasticity offers several attractive properties for the development of tactile sensors: good linearity, compatibility with vision-based sensing technologies, and high spatial resolution associated with the latter. Photoelastic sensors are compatible with fiber-optic technology and, thus, allow remote location of electronic processing devices to avoid interference problems.

Although photoelasticity has been used extensively in the stress analysis of mechanical parts for many years,[1,2] its application to tactile sensing is quite limited. In general, the theory of photoelasticity is well established, photoelastic materials are readily available, and their properties have been tested extensively.[1–4]

One of the earlier applications of photoelasticity to tactile sensing dates back to 1984, to the development phase of the Utah/MIT dexterous hand.[5] The researchers, having not been satisfied with the technologies available for tactile sensing at the time, proposed the use of the photoelastic phenomenon as a transduction method for the recovery of the force profile applied to the fingers of the hand. However, the construction of a large array of their devices would be difficult. To overcome this difficulty, a research group at the University of Oxford proposed a different transducer.[6–8] Although an analytical model for the sensor was proposed by the authors, a systematic method for recovering the force profile from the light-intensity distribution was not reported. Thus, the sensor was used mainly for the study of the forward analysis, namely, observing light intensity distributions (fringes) for different force profiles.

A tactile sensor developed at the University of Wales was reported to be able to detect slippage.[9–11] It is important to note that their analysis does not require the recovery of the applied force profile. Another photoelastic tactile sensor using fiber-optic strain gauges was reported in refs. 12 and 13.

In contrast to other works reported in the literature, this paper presents a comprehensive set of solutions for the forward and inverse problems associated with photoelastic tactile sensors. To achieve this objective, photoelastic tactile sensing must be studied from a general viewpoint. Namely, a basic transducer topology must be selected and its characteristics analyzed. Correspondingly, mathematical models must be created for the inverse problem associated with the sensor, and solution techniques developed.

In Section 2, the forward analysis of a one-layer transducer is detailed, based on the theories of elasticity and photoelasticity. In Section 3, the inverse problem of this transducer is addressed for the case of normal forces under ideal conditions. In Section 4, a two-layer transducer under normal forces is analyzed for nonideal conditions. Finite-element analysis (FEA) is used to model the transducer. A novel algorithm is presented to solve the inverse problem under nonideal conditions. Finally, several conclusions are presented and some recommendations for future work are discussed.

2. ONE-LAYER PHOTOELASTIC TACTILE TRANSDUCER

The photoelastic sensor to be analyzed in the context of this work consists of a set of parallel photoelastic transducer beams, arranged as shown in Figure 1. The force application region consists of a set of tactels onto which line forces are applied. The top of each beam is a mirror surface. Adjacent beams are slightly separated from each other (not shown in Fig. 1) and are assumed to operate independently.

The optical setup proposed for illuminating each transducer is shown in Figure 2. Monochromatic, linearly polarized light is directed toward the photoelastic transducer by a beam splitter. Before reaching the transducer, the light is circularly polarized by a quarter-wave plate. Once the light penetrates the transducer, its polarization is affected by the birefringence induced in the photoelastic element by the forces applied to the transducer. The birefringence creates a phase-lead distribution that transforms the circularly polarized light into elliptically polarized light. A reflecting surface on the back side of the transducer returns the light toward a detector through the quarter-wave plate, the beam splitter, and an analyzer. This setup constitutes a reflective circular polariscope. Finally, the light is detected by

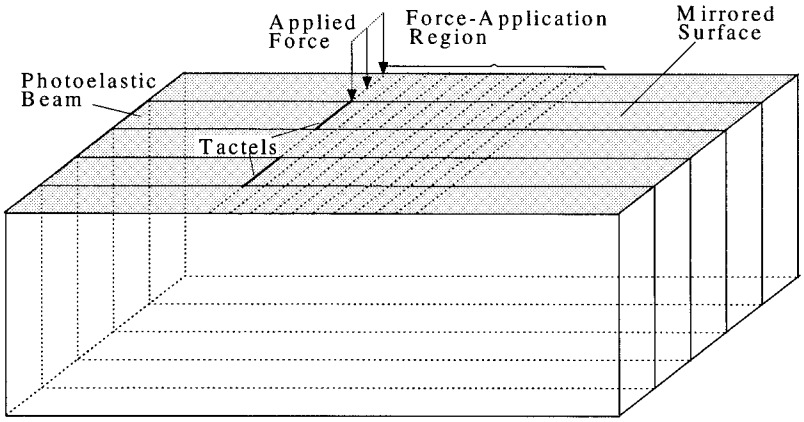

Figure 1. A basic photoelastic tactile sensor.

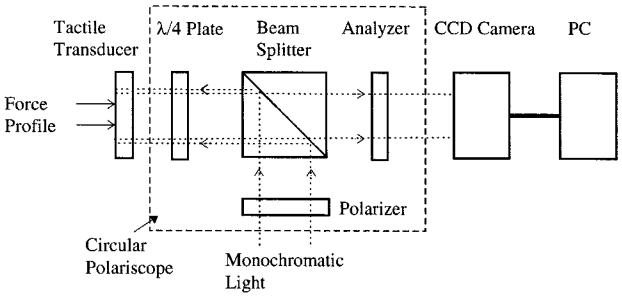

Figure 2. A circular reflective polariscope.

a camera linked to a frame grabber connected to a PC for further data processing. By rearranging the optical elements of the setup, a bright- or a dark-field circular polariscope can be obtained. For the analysis presented in this work, a dark-field polariscope is utilized.

Since the photoelastic beams are not in contact with one another (not shown in Fig. 1), the analysis of each beam can be performed independently. Figure 3 shows a beam of the transducer where the jth tactel is subjected to a normal-line force F_j. The

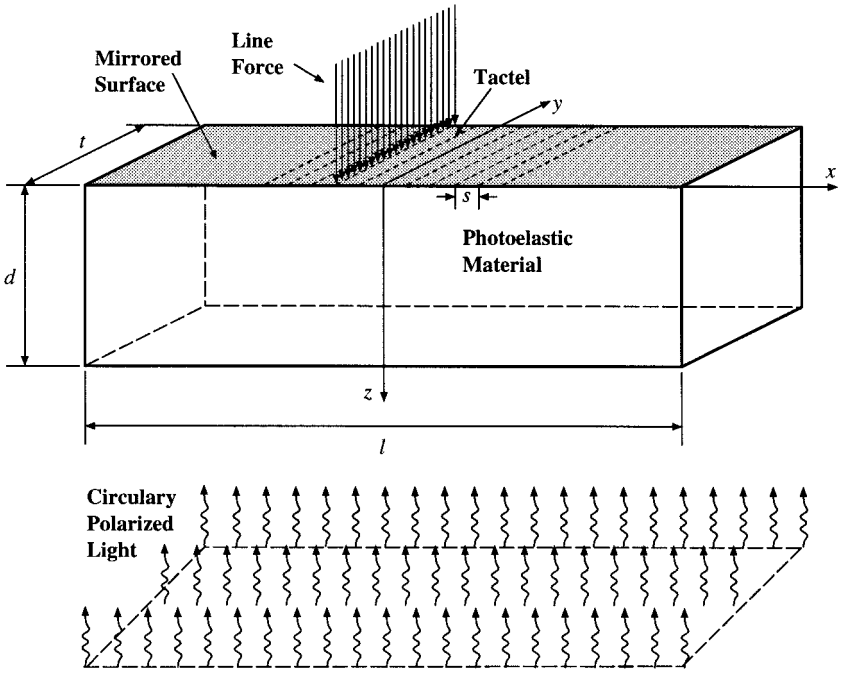

Figure 3. A photoelastic beam of the transducer.

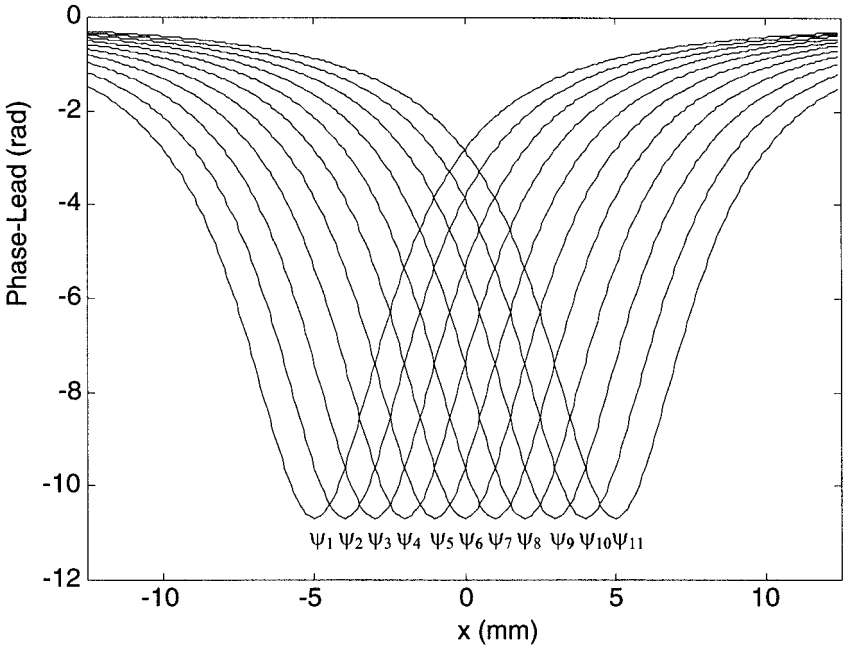

Figure 4. Family of ψ-phase-lead distributions when a load of 1 N is applied.

tactels are separated by equal distances, s, from each other along the x axis.

To find a model for the transducer, it is assumed that the beam can be modeled by an elastic half-space. Note that this assumption represents a first approximation to the real stress distribution created in the transducer and is well established in tactile sensing theory and practice.[14,15] The major advantage of this approximation is that closed-form equation (CFEs) for the phase-lead distribution can be obtained, providing an immediate understanding of the basic parameters that affect the behavior of the sensor.

The phase-lead distribution corresponding to a normal line force, F_j, applied to the jth tactel can be calculated, using the theory of photoelasticity, to be[16]

$$p_j(x) = \psi_j(x) F_j, \tag{1}$$

where

$$\psi_j(x) = -\frac{4K_{ss}}{\pi t} \frac{d^2}{(x - x_j)^2 + d^2}, \tag{2}$$

and x_j is the x coordinate at the jth tactel. In Eq. (2), the function ψ_j can be understood as the phase-lead distribution when a force of 1 N is applied, and depends only on the optomechanical and geometrical properties of the beam. Figure 4 shows a family of ψ_j functions. For this figure, the dimensions and optomechanical parameters of the transducer indicated in Table I were utilized, where E and ν are the modulus of elasticity and Poisson's coefficient of the photoelastic material, l is the length of the transducer, λ is the wavelength of the light, and k_s is the strain-optical coefficient. The stress-optical coefficient, K_{ss}, is given by

$$K_{ss} = \frac{2\pi}{\lambda} \frac{1 + \nu}{E} K_s. \tag{3}$$

When a set of normal line forces is applied at the n_t tactels of the beam and the principle of superposition is utilized, the total phase-lead distribution is given by

$$p(x) = \sum_{j=1}^{n_t} \psi_j(x) F_j. \tag{4}$$

Table I. Dimensions and optomechanical parameters of the transducer

l	t	d	E	ν	λ	K_s	s	n_t
25 mm	2 mm	3 mm	4 MPa	0.49	632.8 nm	0.0045	1 mm	11

If the phase-lead distribution and the functions ψ_j are known at least at n_t points, the recovery of the force profile, in theory, is possible. Unfortunately, the phase-lead distribution cannot be measured directly. When a polariscope is utilized, only the output light intensity can be directly measured. For the case of the dark-field circular polariscope, the output light intensity is given by

$$I(x) = \sin^2 \frac{p(x)}{2}. \tag{5}$$

From Eq. (5) it can be seen that if the phase-lead distribution is between 0 and $-\pi$, for example, the phase-lead distribution can be easily obtained. Now if the phase lead lies outside this range, recovery of the phase-lead distribution from the light intensity distribution becomes difficult, since simple inversion of Eq. (5) does not provide the correct phase-lead distribution. In practice, the phase lead may lie outside the interval $[0 \ -\pi]$, creating the need for the development of a special algorithm capable of properly inverting Eq. (5).

3. PHASE-LEAD RECOVERY UNDER IDEAL CONDITIONS

In this section, the phase-lead distribution of the photoelastic transducer under stress is recovered under ''ideal'' conditions. For our analysis, by ideal conditions, it is implied that the light-intensity distribution can be detected on a continuous intensity scale, namely as a continuous function along the x axis, and that it is noise-free. These conditions simplify the recovery of the phase-lead distribution and, as will be explained in the following sections, allow the development of an algorithm to recover the phase-lead distribution. The nonideal case, which better models the behavior of a real sensor, will be presented in Section 4.

3.1. Forward Analysis

The forward analysis of the sensor consists of analyzing the effect of an applied force profile on the light intensity distribution. This analysis can be performed using Eqs. (2) and (4) in calculating the phase-lead distribution, and Eq. (5) in determining the light intensity distribution. For the exemplary force profile shown in Figure 5 (Example 1), the corresponding phase-lead and light intensity distributions can be determined as shown in Figures 6 and 7, respectively, where the dimensions and optomechanical parameters of Table I are used in the calculations.

3.2. A Generic Phase-Lead Recovery Method

In this section, an algorithm is detailed for recovering the phase-lead distribution from the light intensity distribution. The algorithm requires ''full analysis'' of the light intensity distribution. By full

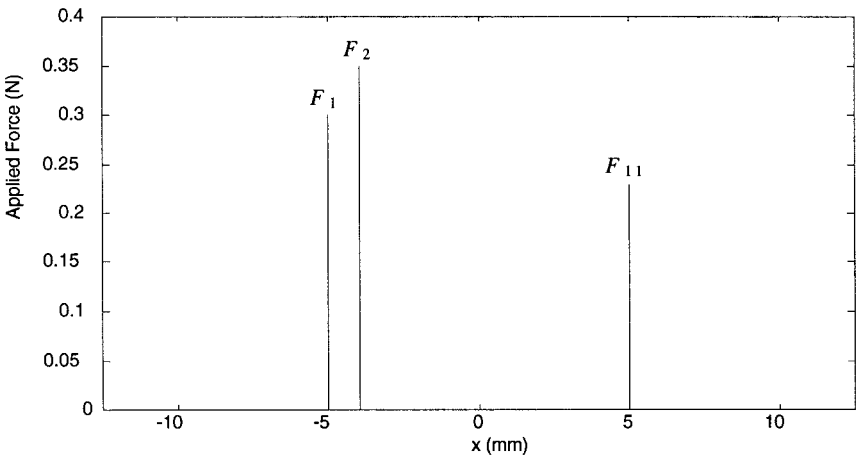

Figure 5. Force profile applied to the transducer for Example 1.

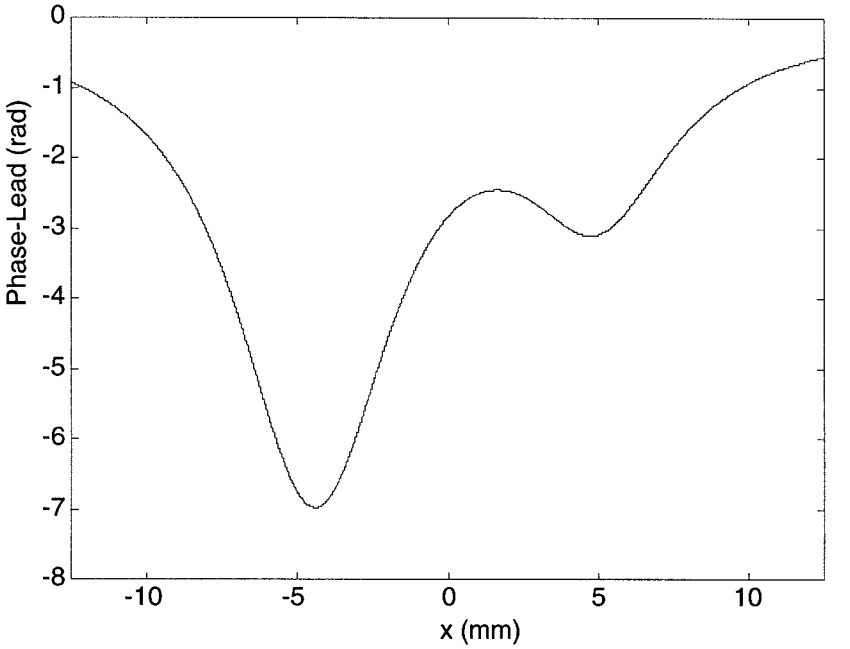

Figure 6. Phase-lead distribution for the force profile of Example 1.

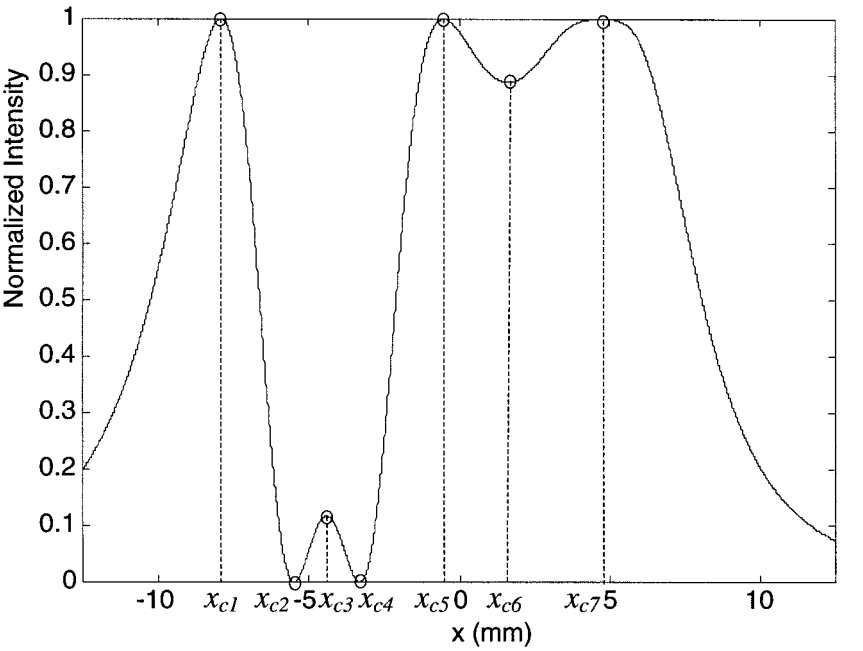

Figure 7. Light intensity distribution for the force profile of Example 1.

analysis, a classification of the *critical points* of the light intensity distribution using high-order derivatives is implied.

3.2.1. Critical Points of the Light Intensity Distribution

The normalized light-intensity distribution is given by (5). Differentiating (5) yields

$$\frac{dI}{dx}(x) = \frac{1}{2}\sin p(x)\frac{dp}{dx}(x). \tag{6}$$

The critical points of $I(x)$ can be found by analyzing $dI/dx = 0$, namely where

$$\sin p(x) = 0, \tag{7.a}$$

and/or

$$\frac{dp}{dx}(x) = 0. \tag{7.b}$$

The critical points of $I(x)$ are indicated herein by x_{ci}, $i = 1, 2, \ldots, n_c$, where n_c indicates the total number of critical points. Equation (7.a) simply indicates that the phase lead is zero or a multiple of π, and (7.b) determines the critical point of $p(x)$. It should be noted that some critical points can satisfy (7.a) and (7.b) simultaneously. These particular points are the ones that complicate the recovery of the phase-lead distribution. The critical points that satisfy (7.a) correspond to the situation in which p equals 0 or a multiple of π. The light-intensity distribution for these points is 0 or 1. Equation (7.b) recovers critical points of the phase-lead distribution. This, in turn, can be used to get specific information about the phase-lead distribution.

The algorithm that recovers the phase-lead distribution from the light-intensity distribution will be explained using Example 1. The critical points of the light-intensity distribution of Example 1 are shown in Figure 7.

3.2.2. Initial Classification of the Critical Points

The critical points of $I(x)$ are classified as those with I equal to one or zero, and those with intensities different from one or zero. The latter points satisfy only (7.b) and are critical points of the phase-lead distribution. In summary, the critical points of $I(x)$ can be classified into three categories:

1. Those that satisfy $I(x_{ci}) = 1$, hereafter referred to as the *ones*, o_j, with $j = 1, 2, \ldots$. In our example, $o_1 = x_{c1}$, $o_2 = x_{c5}$, and $o_3 = x_{c7}$.
2. Those that satisfy $I(x_{ci}) = 0$, hereafter referred to as the *zeros*, z_j, with $j = 1, 2, \ldots$. In our example, $z_1 = x_{c2}$, and $z_2 = x_{c4}$.
3. Those that satisfy $I(x_{ci}) \neq 1$ and $I(x_{ci}) \neq 0$, hereafter referred as *direct critical points of* $p(x)$, c_j, $j = 1, 2, \ldots$. In our example, $c_1 = x_{c3}$, and $c_2 = x_{c6}$.

3.2.3. Finding the Critical Points of the Phase-Lead Distribution

In the previous section, only the critical points of $p(x)$ with associated light intensities different from zero or one were found. In this section, the critical points of $p(x)$, at which the light intensity is one or zero, hereafter referred as *indirect critical points of* $p(x)$, are found.

To find the indirect critical points of $p(x)$, it is necessary to analyze the second derivative of $I(x)$, given by

$$\frac{d^2I}{dx^2} = \frac{1}{2}\sin p\frac{d^2p}{dx^2} + \frac{1}{2}\cos p\left(\frac{dp}{dx}\right)^2. \tag{8}$$

For the case of ones or zeros (where $\sin p = 0$), the second derivative reduces to

$$\frac{d^2I}{dx^2} = \frac{1}{2}\cos p\left(\frac{dp}{dx}\right)^2. \tag{9}$$

If, for the zero or one being analyzed, $d^2I/dx^2 = 0$, then that zero or one is an indirect critical point of p. In our example, it was determined that o_3 is an indirect critical point of p.

3.2.4. Classification of the Critical Points of the Phase-Lead Distribution

The critical points of p must be classified into points of inflection and local extrema, using higher-order derivatives of the light-intensity distribution. In this way, the direct and indirect critical points are separated.

1. For direct critical points of p (where $dp/dx = 0$), the second derivative reduces to

$$\frac{d^2I}{dx^2} = \frac{1}{2}\sin p\frac{d^2p}{dx^2}. \tag{10}$$

If $d^2I/dx^2 \neq 0$, then the point being analyzed corresponds to a local extremum. If $d^2I/dx^2 = 0$, then the third derivative, given by

$$\frac{d^3I}{dx^3} = \frac{1}{2}\sin p\left[\frac{d^3p}{dx^3} - \left(\frac{dp}{dx}\right)^3\right] + \frac{3}{2}\cos p\frac{d^2p}{dx^2}\frac{dp}{dx}, \quad (11)$$

must be analyzed. For the case under analysis, the third derivative reduces to

$$\frac{d^3I}{dx^3} = \frac{1}{2}\sin p\frac{d^3p}{dx^3}. \quad (12)$$

If $d^3I/dx^3 \neq 0$, then the direct critical point of p is an inflection point. If $d^3I/dx^3 = 0$, the fourth derivative of I must be analyzed. In general, it can be proved that analyzing higher derivatives of I at a direct critical point is equivalent to analyzing the higher derivatives of p at the same point. This means that

$$\frac{d^kI}{dx^k} \propto \frac{d^kp}{dx^k}. \quad (13)$$

Thus, if the order of the next nonzero derivative of I at a direct critical point is even, the point that is being analyzed corresponds to a local extremum; if it is odd, the point is an inflection point. In our example, it was found that c_1 and c_2 correspond to local extrema.

2. For indirect critical points of p (where $\sin p = 0$ and $dp/dx = 0$), the second derivative is zero, and the third derivative also reduces to zero. Thus, the fourth derivative must be analyzed. It can be proved that, for the case under study, the fourth derivative reduces to

$$\frac{d^4I}{dx^4} = \frac{3}{2}\cos p\left(\frac{d^2p}{dx^2}\right)^2. \quad (14)$$

If $d^4I/dx^4 \neq 0$, the indirect critical point under study corresponds to a local extremum on the phase-lead distribution. If $d^4I/dx^4 = 0$, the next nonzero derivative must be analyzed. In our case, it is even and of the form

$$\frac{d^{2k}I}{dx^{2k}} \propto \left(\frac{d^kp}{dx^k}\right)^2. \quad (15)$$

If $d^{2k}I/dx^{2k} \neq 0$ and k is even, the point under analysis corresponds to a local extremum on the phase-lead distribution; if k is odd, it is an inflection point.

At this stage, all of the critical points of p have been classified as inflection points or local extrema. It is also noted that it is not necessary to know whether the local extrema are maxima or minima.

For our example it was determined that o_3 is a local extremum of p.

3.2.5. A New Classification of Critical Points of the Light Intensity Distribution

Following the analysis just presented, a new classification of the critical points of I can be performed:

1. *Class 1*: Critical points of $I(x)$, where $I(x) = 1$, and the first nonnegative derivative is of the form $d^{2k+1}I/dx^{2k+1}$ for some integer $k \geq 1$, hereafter designated as κ_i, with $i = 1, 2, \ldots$.
2. *Class 2*: Critical points of $I(x)$, where $I(x) = 0$, and the first nonnegative derivative is of the form $d^{2k+1}I/dx^{2k+1}$ for some integer $k \geq 1$, hereafter designated as ζ_i, with $i = 1, 2, \ldots$.
3. *Class 3*: Critical points of $I(x)$ which are local extrema but do not satisfy conditions (a) or (b). These points are hereafter designated as χ_i, with $i = 1, 2, \ldots$.

Basically, class 1 points are the previous *ones*, with the exception of all the indirect critical points of p that are local extrema; class 2 points are the previous *zeros*, with the exception of all the indirect critical points of p that are local extrema; finally, class 3 points are the *direct and indirect critical points of p* which are local extrema.

Using this new classification on our example indicates that the class 1 points are $\kappa_1 = o_1$ and $\kappa_2 = o_2$; the class 2 points are $\zeta_1 = z_1$ and $\zeta_2 = z_2$; and the class 3 points are $\chi_1 = c_1$, $\chi_2 = c_2$, and $\chi_3 = o_3$. The new classification of the critical points is shown in Figure 8.

3.2.6. A Comprehensive Algorithm for Phase-Lead Recovery

In the previous subsections, a classification of critical points was performed. Based on this classification and the algorithm described in this subsec-

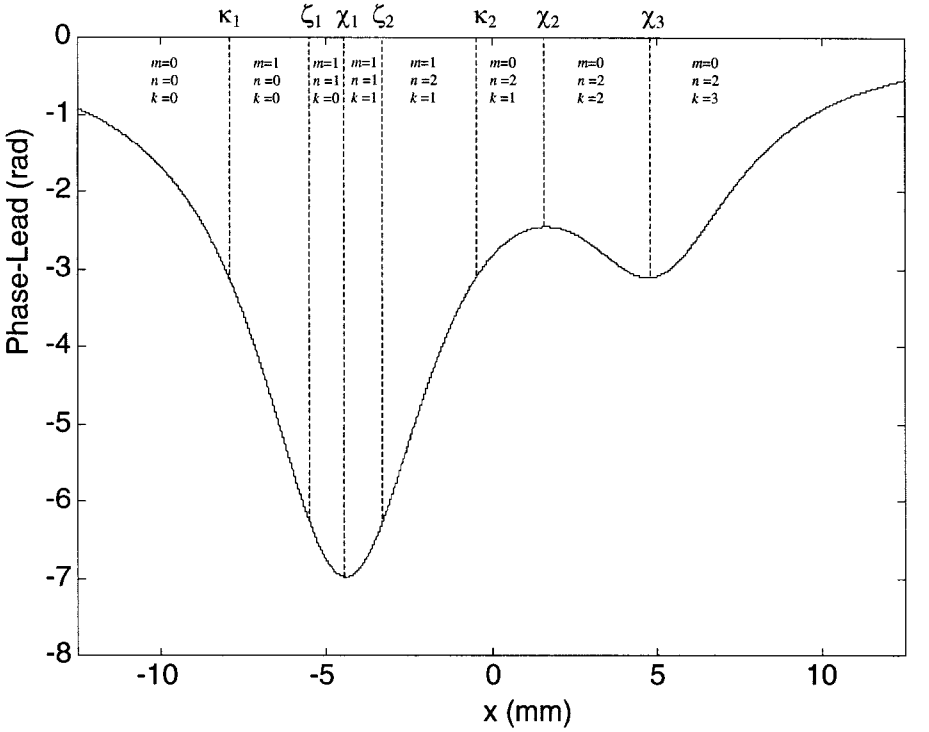

Figure 8. Reconstructed phase-lead distribution for Example 1.

tion, the phase-lead distribution can be recovered uniquely.

Before the algorithm is described, it is interesting to note what kind of information the different critical points can provide. For example, a class 1 or a class 2 critical point indicates that, at that point, the phase-lead is switching from one branch to another of the arcsin function. A class 3 point, on the other hand, indicates that the phase lead reaches an extremum. Immediately before and after the point, the derivatives of the phase lead have different signs.

To fully recover the phase-lead distribution, one must know the value of the phase lead at one point in the interval $\mathbf{v} = [-l/2 \;\; l/2]$. For the present algorithm, it will be assumed that the phase lead at $x = -l/2$ (or $x = l/2$) is known, and that its value is between 0 and $-\pi$. Under this condition, the phase lead can be reconstructed point by point using the following formula:

$$p(x) = -2\pi m - (-1)^{m+n} 2 \arcsin\sqrt{I(x)}\,. \quad (16)$$

The algorithm starts with $m = 0$, $n = 0$, and $k = 0$, and the index m is defined as $m \to m + (-1)^k$. The phase-lead distribution is recovered point by point, increasing x from $-l/2$ to $l/2$ (or vice versa). When a class 3 critical point is encountered, k is increased by one; when a class 2 critical point is encountered, n is increased by one; and, when a class 1 critical point is encountered, m is increased or decreased by one, depending on the value of k.

In Figure 8, the steps in the reconstruction of the phase-lead distribution are shown. The sections of the curve with the same parameters m, n, and k are indicated, as well as the different critical points.

One of the major problems with the algorithm previously described is the need for the analytical expressions for the light intensity distribution to calculate the high-order derivatives with accuracy. However, as will be seen in the next section, measurements of the light intensity distribution are subject to electronic noise, quantization error, and sampling error, which make the calculation of derivatives impossible to the extent required by the algorithm. If the high-order derivatives cannot be calculated, then the classification of the critical points cannot be performed accurately, and the inverse problem (of finding the phase-lead distribution) becomes ill posed. In Section 4, a study of the

recovery of the phase-lead distribution under ill-posed conditions is performed.

4. ANALYSIS OF A TWO-LAYER TRANSDUCER

In the transducer topology described in Section 2 and analyzed in Section 3, a practical problem exists: the grasped object would be in direct contact with the mirrored surface of the transducer. This would eventually damage the mirrored surface and, consequently, cause a deterioration of the output light from the polariscope. Thus, it seems evident that a compliant protective layer is needed for the development of a robust transducer (Fig. 9). Note that the mechanical properties of the photoelastic and the compliant layers can be different.

In general, the forward analysis performed in Section 2 is still valid for the new transducer, except that the shapes of the phase-lead distributions are affected by the compliant layer. Moreover, since the generic method for the recovery of the phase-lead distribution, described in Section 3, is independent of the particular dimensions, optomechanical properties, and structure of the transducer, the phase-lead distribution can be recovered with this method if the ideal conditions are assumed to apply for this case. Thus, we limit our discussion to the forward analysis of the transducer under ideal conditions. In this paper, the modeling of the transducer is performed by finite-element analysis (FEA). However, in ref. 17, the forward analysis using CFEs was presented for a two-layer transducer, in which both layers have the same mechanical properties.

Furthermore, the light intensity distribution of a real sensor is susceptible to noise. Under these conditions, the method reported in Section 3 cannot be applied directly to the recovery of the phase-lead distribution because the inverse problem becomes ill-posed. In response to this difficulty, an alternative method is developed for the recovery of the phase-lead distribution.

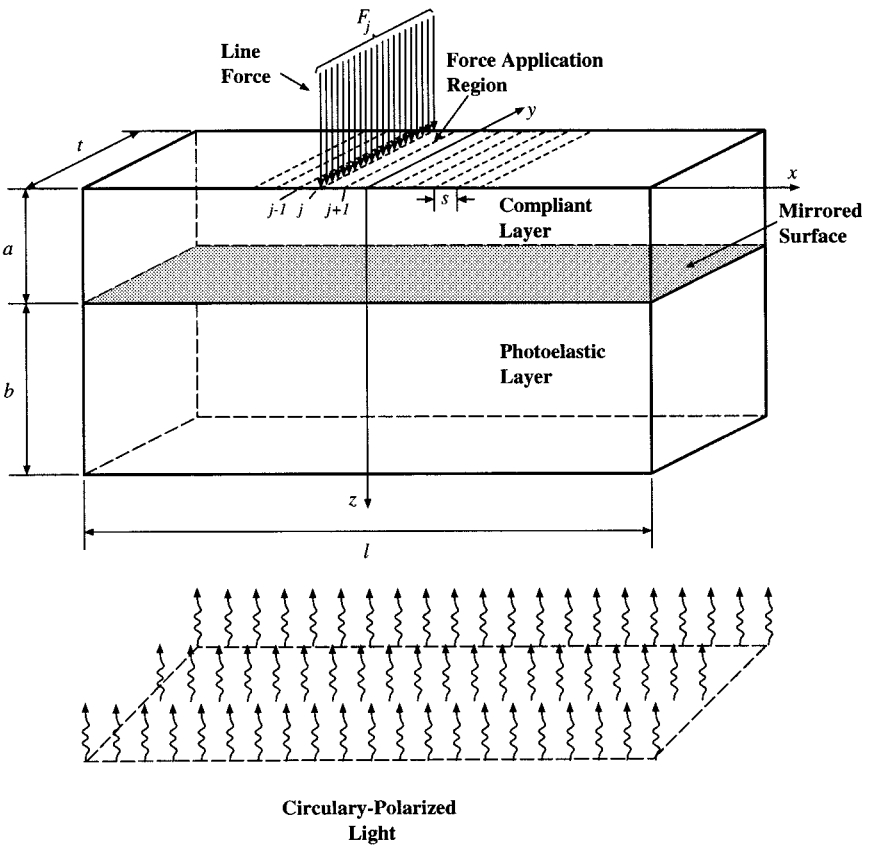

Figure 9. An element of the two-layer photoelastic tactile transducer.

4.1. FEA Analysis of the Proposed Transducer

The phase-lead distribution $p(x)$ for the two-layer transducer can be calculated as[16]

$$p(x) = 2K_{ss}\int_{a}^{a+b} \sigma_x(x, z)\, dz, \qquad (17)$$

where the calculation of the 2-D shear stress distribution in the photoelastic transducer, $\sigma_x(x, z)$, is carried out by FEA.

4.1.1. Boundary Conditions

The stress distribution is directly related to the boundary conditions (BCs) of the transducer: those shown in Figure 10a are denoted by BC1, and the ones in Figure 10b by BC2. For BC1, the theory of elasticity establishes that the stress distribution values at $x = -l/2$ and $x = l/2$ must be zero, since no forces are applied to the lateral borders of the transducer. For BC2, on the other hand, the stresses do not necessarily have to be zero at $x = -l/2$ and $x = l/2$.

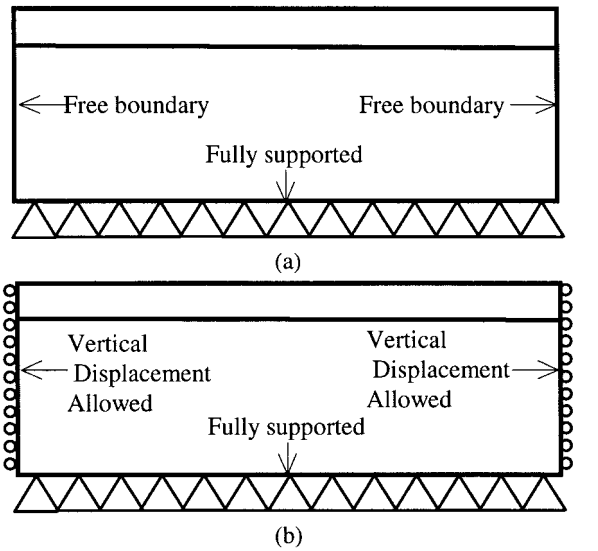

Figure 10. Boundary conditions.

4.1.2. General Analysis of the Transducer by FEA

The first step in calculating the stresses consists of establishing a mesh characterizing the photoelastic transducer (Fig. 11). In our case, the central part of the mesh was configured to have more elements than the outer parts, to improve the accuracy of the stress calculations in the central region, where the forces are applied and the stress gradients are higher. For the same reason, the photoelastic layer has more elements than the region corresponding to the compliant layer. E_1 and E_2, and ν_1 and ν_2 denote the modulii of elasticity and Poisson's coefficients of the compliant and the photoelastic layers, respectively. Δx_1 and Δx_2 are the widths of the elements along the x axis, in the central and outer regions, respectively. Δz_1 and Δz_2 represent the heights of the elements along the z axis, in the compliant and photoelastic layers, respectively. The numbers of nodes along the x axis in the central and outer regions are denoted by m_{1n} and m_{2n}. The total number of these elements is denoted by $m_n = m_{1n} + m_{2n}$. The number of nodes along the z axis in the compliant and the photoelastic layer is indicated by l_{1n} and l_{2n}, respectively.

In all of the examples presented in this section, it is assumed that the materials of both layers of the

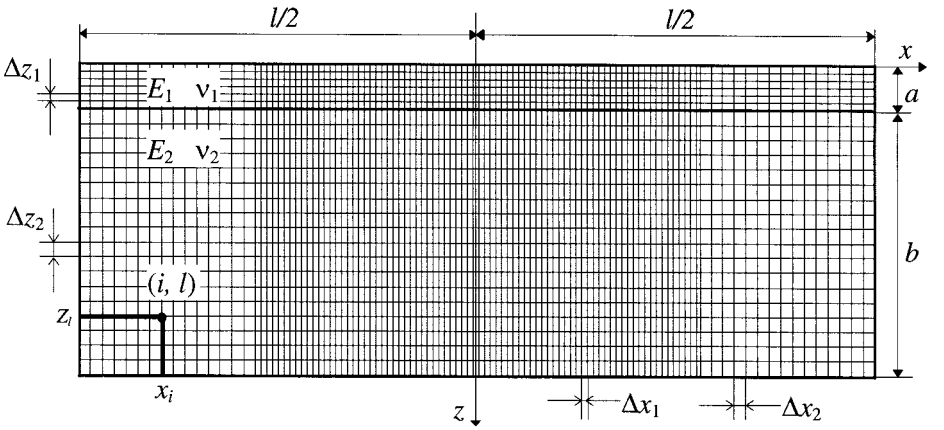

Figure 11. Finite-element mesh representation for the transducer.

transducer work in the linear-elastic region, that the forces are applied only at the tactels (see Fig. 9), and that plane stress conditions apply.[19]

Since stresses are calculated by FEA at each of the nodes of the mesh, Eq. (17) is rewritten as

$$p_i = 2K_{ss} \sum_{l=1}^{l_{2n}} \sigma_{il} \Delta z_2, \tag{18}$$

where p_i is the phase lead at x_i, σ_{il} is the shear stress at the node (i, l), and l_{2n}, as indicated before, is the number of nodes along the x_i coordinate inside the photoelastic layer. Applying the principle of superposition to stresses, one can easily prove that the phase-lead distribution can be rewritten as[16]

$$p(x_i) = \frac{1}{W} \sum_{j=1}^{n_t} \psi_j(x_i) F_j, \tag{19}$$

where ψ_j is the corresponding phase-lead distribution when a load W is applied at the jth tactel, F_j is the magnitude of the force, and n_t is the number of tactels. The family of ψ-functions completely characterizes the transducer since, if they are known, the phase-lead distribution corresponding to any force profile can be obtained by applying (19). Even though, in this paper, force profiles with only normal components are considered, in general, it is possible to perform the analysis with force profiles with tangential components.[18] The force profile must be narrower than the length of the transducer (x axis).

The effect of BCs in the response of the sensor is presented by using a new example (Example 2). For this example, it is assumed that a 0.1 N force is applied to each tactel. The transducer for Example 2 is defined by Table II and the mesh is defined by Table III.

Figure 12 shows the phase-lead distributions for a transducer under BC1 and BC2. As can be observed, the phase-lead distribution at the borders are different because of the BCs. In the case of BC1, the shear stress distribution is zero, and correspondingly, the phase-lead distribution must be zero. However, as can be observed in Figure 13, the phase-lead distribution is not exactly zero at the borders because of small numerical errors in the calculation of the shear stress at the borders. In Figure 12, the phase-lead distribution is not zero, because of the effect of the rollers that creates shear stresses at the borders. Note that BC1 always satisfies the condition that the phase-lead distributions at $x = -l/2$ and $x = l/2$ are in the interval $[0 \ -\pi]$, since $p(l/2) = p(-l/2) = 0$. However, the phase-lead distribution corresponding to BC2 does not necessarily satisfy this condition, since the phase leads at the borders depend on the magnitude of the force profile. Consequently, a transducer under BC1 has an a priori larger dynamic range than the one under BC2.[16,18]

4.2. Analysis under Nonideal Conditions

To show the robustness of our method, the analyses are presented herein through yet another example (Example 3), in which a different force profile is applied to the transducer defined for Example 2.

4.2.1. Forward Analysis under Ideal Conditions

The force profile applied to the transducer is shown in Figure 13. After calculating the stress distribution by FEA for BC1 and applying (18), the resulting

Table II. Dimensions and parameters of the transducer

l	t	a	b	s	E_1	E_2	ν_1	ν_2	λ	K_s	n_t
25 mm	2 mm	0.5 mm	3 mm	1 mm	110 MPa	1.1 GPa	0.49	0.42	632.8 nm	0.0025	11

Table III. Dimensions and number of nodes of the mesh in each region

Δx_1	Δx_2	Δz_1	Δz_2	m_{1n}	m_{2n}	l_{1n}	l_{2n}
83.3 μm	343.75 μm	83.33 μm	186.66 μm	167	34	6	19

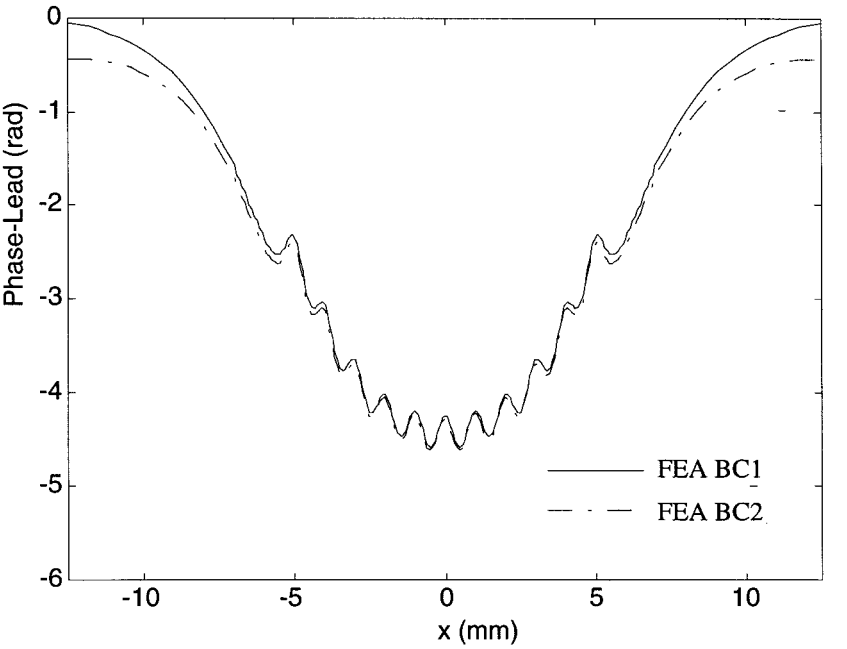

Figure 12. Phase-lead distributions for Example 2 under BC1.

phase-lead distribution is as shown in Figure 14. The continuous line in Figure 14 represents a linear interpolation of the 201 consecutive points. The output normalized light intensity distribution of the polariscope can be calculated using (5) (Fig. 15).

4.2.2. Forward Analysis under Nonideal Conditions

A typical detection process involved in the evaluation of the output light intensity of the polariscope is shown in Figure 16. The output light from the polariscope can be detected by a CCD linear array with an active length equal to the length of the transducer and aligned perpendicular to the direction of propagation of the light. Note that, for this case, a linear array can be used as a detection device because only one transducer beam is analyzed. Subsequently, the analog electrical signal generated by the CCD array is processed and finally transformed by an A/D converter into digital form for further

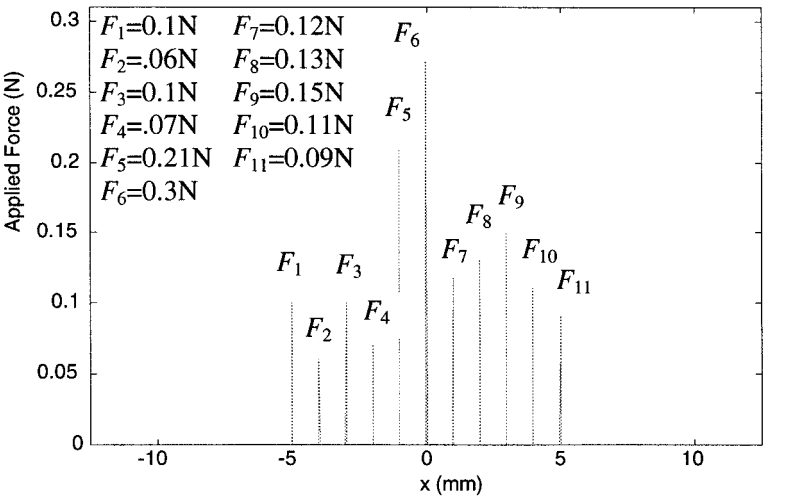

Figure 13. Applied force profile for Example 3.

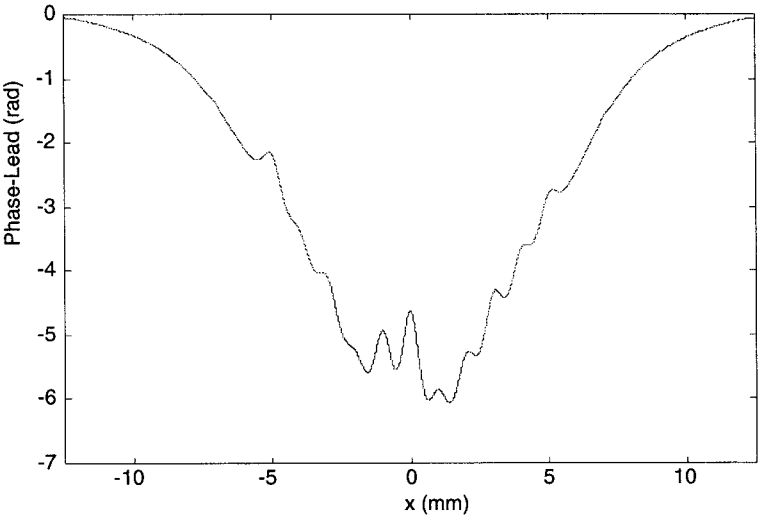

Figure 14. Phase-lead distribution for Example 3.

data processing with a PC. Since the linear array samples the light intensity distribution in pixel-quantized space, Eq. (5) can be rewritten in discrete form as

$$I(x_i) = \sin\frac{p(x_i)}{2} \qquad \text{for } i = 1, 2, \ldots m_{\mathrm{p}}, \quad (20)$$

where m_{p} is the number of pixels in the linear array.

The equations for $p(x)$ and ψ_j, respectively, can also be rewritten in a discrete form as

$$P_i = p(x_i) \qquad \text{for } i = 1, 2, \ldots m_{\mathrm{p}}, \quad (21)$$

$$\psi_{ij} = \psi_j(x_i) \qquad \text{for } i = 1, 2 \ldots m_{\mathrm{p}};\ j = 1, 2 \ldots n_{\mathrm{t}}. \quad (22)$$

The discrete version of Eq. (4) can, thus, be rewritten in matrix notation as

$$\mathbf{P} = \frac{\mathbf{1}}{\mathbf{W}} \mathbf{\Psi}\, \mathbf{F}, \quad (23)$$

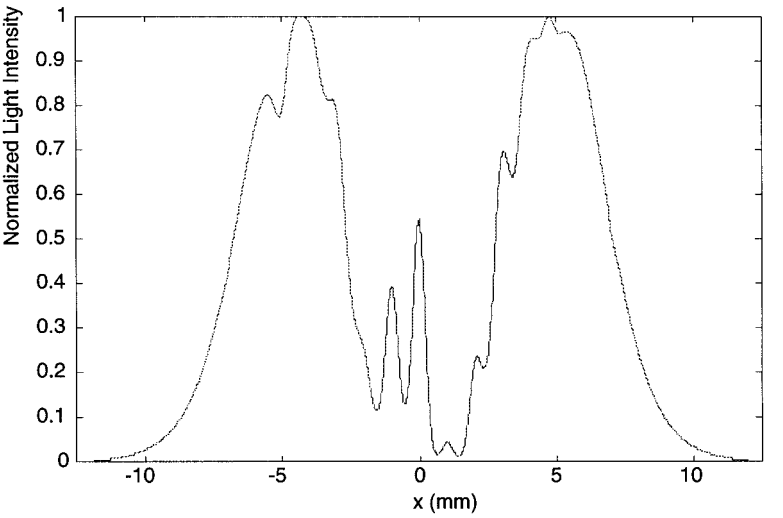

Figure 15. Normalized light intensity distribution for Example 3.

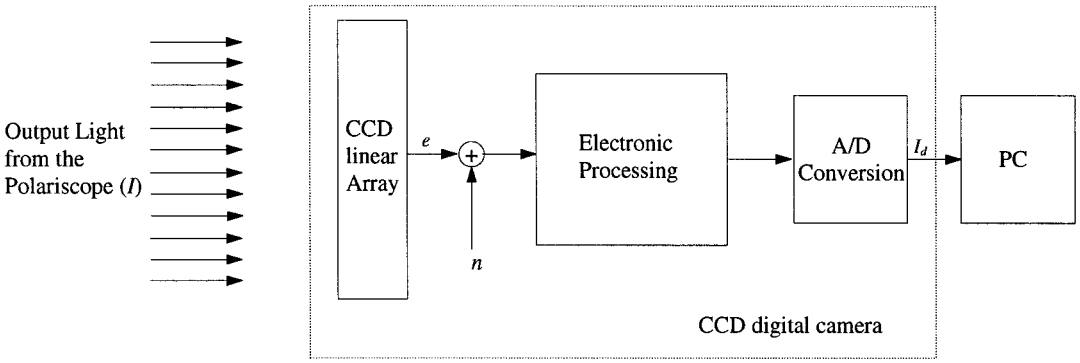

Figure 16. Detection and processing of the output light intensity.

where

$$\mathbf{P} = \begin{bmatrix} P_1 \\ P_2 \\ \vdots \\ P_{m_p} \end{bmatrix};$$

$$\boldsymbol{\psi} = \begin{bmatrix} \psi_{11} & \psi_{12} & \cdots & \psi_{1n_t} \\ \psi_{21} & \psi_{22} & \cdots & \psi_{2n_t} \\ \vdots & \vdots & & \vdots \\ \psi_{m_p1} & \psi_{m_p2} & \cdots & \psi_{m_pn_t} \end{bmatrix}; \qquad (24)$$

$$\mathbf{F} = \begin{bmatrix} F_1 \\ F_2 \\ \vdots \\ F_n \end{bmatrix}$$

P is the phase-lead vector, **Ψ** is the model matrix, and **F** is the input force-profile vector.

Once the light intensity has been discretized by the linear array, the measurements are converted into digital form by an A/D converter. Assuming that the A/D converter has a certain number of bits B, the maximum number of grey levels obtainable is 2^B. The A/D converter also introduces quantization noise to the signal. In addition to this noise, random electronic noise, n_o, is herein added to the signal. The effect of the A/D converter is simulated by the function ''round.''[a]

[a] The ''round'' function returns the closest integer to the real number presented to it.

The detected light intensity distribution (in grey levels), I_d, can be written as

$$I_d(x_i) = \text{round}\left[A \sin^2 \frac{p(x_i)}{2} + n_o(x_i) + I_o \right]$$

$$\text{for } i = 1, 2 \ldots m_p, \qquad (25)$$

where $n_o(x_i)$ is the electronic noise introduced into the measurement of the light intensity of the ith pixel; I_o is the minimum average signal applied to the A/D converter, such that $[I_o + \min(n_o)] \geq 0$; and A is the maximum allowed dynamic range of the signal applied to the A/D converter, such that $[A + I_o + \max(n_o)] \leq 2^B - 1$. These two last inequalities are intended to guarantee that the system works in a linear region (for which no distortion is introduced between the incident and detected light intensities).

Continuing with Example 3, and considering the parameters of Table IV (where gl stands for grey-level units), the detected light intensity distribution I_d can be calculated using Eq. (25), as shown in Figure 17.

Figure 17 represents the last step of the forward analysis under nonideal conditions. The phase-lead distribution must be recovered from Eq. (25). However, the critical points of I_d cannot be classified by the method outlined in Section 3, since the derivatives of I_d cannot be calculated with the accuracy required by the algorithm. Thus, a new method that allows us to recover the phase-lead distribution from a ''noisy'' light intensity distribution must be found. Such a method is reported in the following section.

Table IV. Parameters of the detection process

B	I_o	A	n_o (random)
8	5 gl	245 gl	−5 gl to 5 gl

4.3. Inverse Analysis under Nonideal Conditions

In this section, a method for recovering the phase-lead distribution from a ''noisy'' light-intensity distribution is explained. For purposes of clarity, the method is presented through Example 3.

4.3.1. Spatial Filtering of the Light Intensity

To reduce the noise in the detected light intensity distribution, the digital data I_d are filtered with an ideal low-pass filter implemented at the software level. This filter was selected by means of a large number of simulations. In each simulation, a ''noisy'' light-intensity distribution (with -5 to 5 grey levels of random noise) was calculated for a given force profile, and subsequently, it was filtered with a range of ideal low-pass filters having different pass-bands. From these results a filter, the pass-band of which is 200 μm^{-1} and which cuts the noise significantly without producing noticeable distortion in the light-intensity distribution, was selected. With this filter, the noise is reduced approximately to the range of -2 to 2 grey levels, from the -5 to 5 originally introduced into the light intensity distribution used in the simulations. The final step consisted of normalizing the filtered light intensity distribution by dividing it by 2^B (in our example, 255). The normalized filtered light intensity distribution, I_f, for the example under analysis is shown in Figure 18.

The phase-lead distribution must be recovered from I_f, in which case, I_f can be written as

$$I_f(x_i) = \sin^2 \frac{p_n(x_i)}{2}, \tag{26}$$

where p_n is the noisy phase-lead distribution. Note that it is p_n (not p) that will be recovered.

4.3.2. Classification of the Critical Points

The critical points of the normalized filtered light-intensity distribution are found next. For Example 3, there are 19 critical points, denoted by c_k, $k = 1, 2 \ldots 19$ (Figure 18). The next step is to classify the critical points. As explained before, the classification used in Section 3 is not applicable here. Accordingly, a new approach must be found to classify the critical points, based on the fact that a strict classification of the critical points into the class 1, class 2, and class 3 categories of critical points cannot be performed directly.

Rather, the normalized filtered light intensity ditribution is divided into three regions: region 1, where $0.98 \le I \le 1$; region 2, where $0 < I < 0.02$; and region 3, where $0.02 \le I \le 0.98$. The widths of regions 1 and 2 were obtained, approximately, by

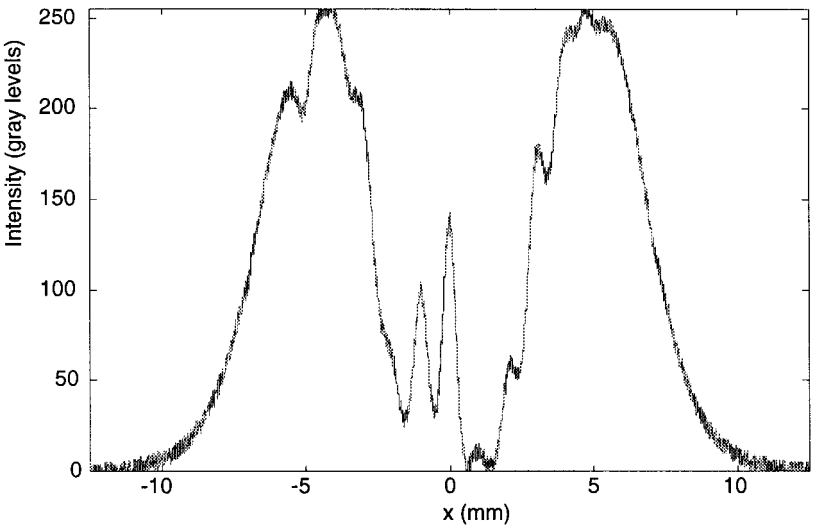

Figure 17. Detected light intensity distribution.

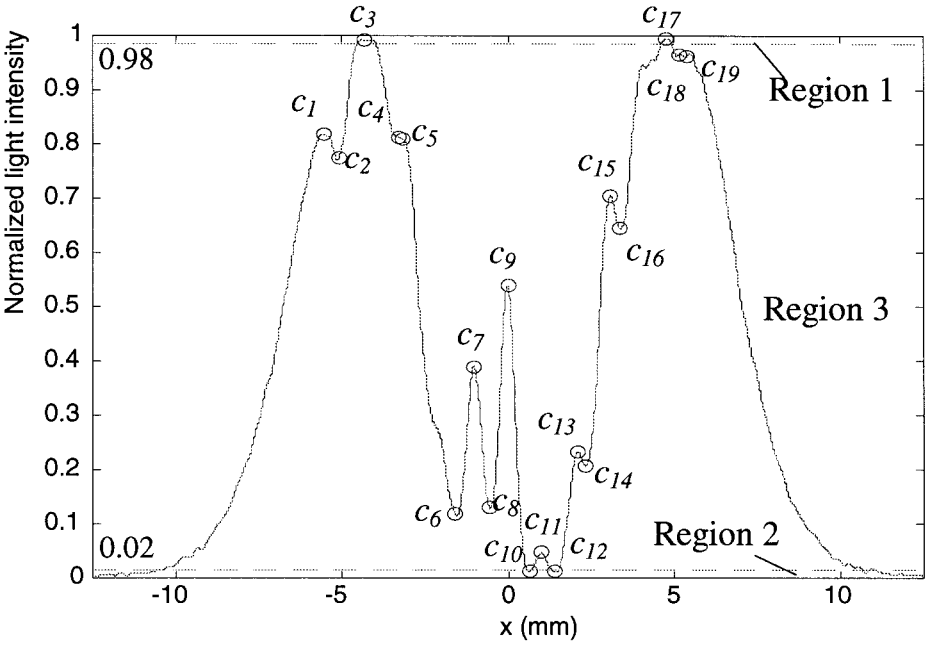

Figure 18. Normalized filtered light intensity distribution for Example 3.

dividing the maximum noise swing after filtering (4 grey levels) in the filtered light intensity distribution by A (i.e., $4/245 \sim 0.02$).

The critical points are now classified as follows:

1. All *local extrema* in region 1 are either class 1 or class 3 points.
2. All *local extrema* in region 2 are either class 2 or class 3 points.
3. All *local extrema* in region 3 are class 3 points.

In our example, c_3 and c_{17} are in region 1, and c_{10} and c_{12} are in region 2. The rest of the local extrema are in region 3.

Because of uncertainty about the class of critical points in region 1 and 2, several different phase-lead distributions can be recovered by using the algorithm outlined in Section 3, of which only one is correct. This constitutes, in essence, an ill-posed inverse problem. Namely, each local extremum in regions 1 and 2 would yield two possible phase-lead distributions. If the total number of local extrema in regions 1 and 2 is C, then the total number of possible phase-lead distributions is 2^c. In our example $C = 3$, leading to eight possible phase-lead distributions. In Table V, the complete set of possible cases is shown, in which, for coding purposes, the number ''1'' is assigned to class 1 critical points,

Table V. Sets of possible critical points

Case no.	c_1	c_2	c_3	c_4 to c_{11}	c_{12}	c_{13} to c_{16}	c_{17}	c_{18}	c_{19}
1	0	0	0	0	0	0	0	0	0
2	0	0	0	0	0	0	1	0	0
3	0	0	0	0	−1	0	0	0	0
4	0	0	0	0	−1	0	1	0	0
5	0	0	1	0	0	0	0	0	0
6	0	0	1	0	0	0	1	0	0
7	0	0	1	0	−1	0	0	0	0
8	0	0	1	0	−1	0	1	0	0

"−1" to class 2 critical points, and "0" to class 3 critical points.

4.3.3. Minimization of the Possible Sets of Critical Points

The number of possible phase-lead distributions grows exponentially with the number of local extrema in regions 1 and 2. Correspondingly, to reduce the computational time involved in recovering each phase-lead distribution, the number of possible cases must be reduced.

The first approach used consists of reducing the width of regions 1 and 2 as much as possible. However, there exists a minimum width, such that if the width is reduced further, errors will occur in the categorization of the critical points and, consequently, the sought phase-lead distribution will not be found, because the correct set of critical points has been eliminated. Thus, a conservative approach is desirable in selecting the widths of regions 1 and 2 to avoid errors in the event that the actual magnitude of noise exceeds the estimated one.

Another approach to reducing the number of spurious phase-lead distributions consists of checking all of the cases with respect to a set of verification rules based on the general properties of such phase-lead distributions. This set of rules can be summarized as follows:

Rule 1. If c_{k1} and c_{k2} are both class 1 or both class 2 critical points, such that between them only class 3 critical points exist, then the number of such class 3 critical points must be odd.

Rule 2. If c_{k1} is a class 1 (class 2) critical point and c_{k2} is a class 2 (class 1) critical point, such that between them only class 3 critical points exist, then the number of such class 3 critical points must be even.

Rule 3. If c_{k1} and c_{k2} are two consecutive critical points, they cannot both be class 1 or class 2 critical points.

Rule 4. The parameter m in Eq. (16) must be zero for $x = -l/2$ and $x = l/2$. This implies a certain symmetry in the distribution of critical points.

After the above rules are applied to Table V, the number of cases is reduced to three, as shown in Table VI. For example, case 2 violates rule 4, and case 4 violates rule 2. Some cases can violate more than one rule. However, in the algorithm, the rules are implemented sequentially. If a case violates one rule, it is immediately eliminated. To optimize the method and diminish the computational time involved in applying the verification rules, the rules that statistically eliminate more cases should be checked first. Rule 4 is the one that, in general, eliminates the most cases. In ref. 16, a practical implementation of the rules is detailed.

4.3.4. Phase-Lead Reconstruction and Testing

Once the number of possible sets of critical points has been reduced by applying the rules described in the previous section, the next step consists of the recovery of the phase-lead distribution corresponding to each set, using the algorithm described in Section 3. Since only one of these distributions is the one sought, the spurious phase-lead distributions must be eliminated.

To recover the input force profile from Eq. (23), one would need to know the phase-lead vector $\mathbf{P}$ and the model matrix $\mathbf{\Psi}$. Although a model matrix $\mathbf{\Psi}$, based on an approximate model of the transducer, could be obtained, it is not advisable to use this approximation in solving the inverse problem of a real sensor, since the model could not be completely accurate. For that reason, it is better to work with measured ψ-functions. Since in this study, we are not making real measurements, the ψ-functions should be similar to the ones provided by the model, except for the simulated noise introduced into them. These ψ-functions are indicated by $\hat{\psi}$ (the

Table VI. The reduced set of possible critical points after the verification rules are applied

Case no.	c_1	c_2	c_3	c_4 to c_{11}	c_{12}	c_{13} to c_{16}	c_{17}	c_{18}	c_{19}
1	0	0	0	0	0	0	0	0	0
3	0	0	0	0	−1	0	0	0	0
6	0	0	1	0	0	0	1	0	0

symbol ^ above Ψ is used to indicate noisy conditons) and can be calculated by

$$\hat{\psi}_j(x_i) = -2\arcsin\sqrt{I_{\mathrm{fj}}(x_i)} \qquad \text{for } j = 1, 2, \ldots, n_{\mathrm{t}}, \tag{27}$$

where I_{fj} is the corresponding normalized filtered light intensity distribution, when a load W is applied to the jth tactel. It must be noted that W should be empirically determined to yield only class 3 critical points in the light intensity distribution so that Eq. (27) provides the right phase-lead distribution. In the measurement process, this step corresponds to the calibration of the transducer.

Grouping the $\hat{\psi}$-functions as was done for Eq. (23), the model matrix under nonideal conditions, $\hat{\mathbf{\Psi}}$, is obtained. The relation equivalent to Eq. (23) is given by

$$\mathbf{P}_{\mathrm{n}} \cong \frac{1}{W}\hat{\mathbf{\Psi}}\,\mathbf{F}, \tag{28}$$

where $\mathbf{P}_{\mathrm{n}}$ is the noisy phase-lead vector. The normalization factor, W, is present because in calculating the $\hat{\psi}$-functions, it is not necessarily assumed that a 1 N force is applied to each tactel. Furthermore, since nonideal conditions apply, the relationship constitutes an approximation.

In this section, an algorithm is detailed with which to find the correct phase-lead vector among the reduced set of phase-lead vectors. The algorithm consists of the following steps:

1. The phase-lead vector corresponding to each of the cases, obtained after applying the rules previously described, is recovered by using the algorithm reported in Section 3. The recovered phase-lead vectors are denoted by $\mathbf{P}_{\mathrm{r}}$.
2. The associated force profile $\mathbf{F}_{\mathrm{r}}$, for each $\mathbf{P}_{\mathrm{r}}$, is obtained by solving Eq. (28) for $\mathbf{F}$. In our case, the following nonnegative, least-squares problem was formulated and solved:

$$\min_{\mathbf{F}_{\mathrm{r}}} \left\| \frac{1}{W}\hat{\mathbf{\Psi}}\,\mathbf{F}_{\mathrm{r}} - \mathbf{P}_{\mathrm{r}} \right\|, \qquad \text{such that } \mathbf{F}_{\mathrm{r}} \geq 0. \tag{29}$$

   The vector $\mathbf{F}_{\mathrm{r}}$ is restricted to being nonnegative because of the positive force profile requirement in our case.[b]

3. An auxiliary phase-lead distribution $\mathbf{P}_{\mathrm{v}}$ is obtained as

$$\mathbf{P}_{\mathrm{v}} = \frac{1}{W}\hat{\mathbf{\Psi}}\,\mathbf{F}_{\mathrm{r}}. \tag{30}$$

   It should be noted that $\mathbf{P}_{\mathrm{v}}$ and $\mathbf{P}_{\mathrm{r}}$ are not necessarily the same or even similar. To understand this possible difference between $\mathbf{P}_{\mathrm{v}}$ and $\mathbf{P}_{\mathrm{r}}$, one should understand that the minimum least-squares problem solved in the previous step gives a force profile, $\mathbf{F}_{\mathrm{r}}$, such that $(1/W)\hat{\mathbf{\Psi}}\,\mathbf{F}_{\mathrm{r}}$ produces the minimum least-squares error in relation to the given $\mathbf{P}_{\mathrm{r}}$. In other words, the solution of Eq. (29) gives the best approximation using the matrix $\hat{\mathbf{\Psi}}$.
4. The true phase-lead distribution is the one in which the difference between $\mathbf{P}_{\mathrm{v}}$ and $\mathbf{P}_{\mathrm{r}}$ is a minimum. This is equivalent to finding the case that produces the minimum percentage error, where

$$\mathrm{Error}(\%) = \frac{1}{\Delta P_{\max}} \max\{\mathrm{abs}[\mathbf{P}_{\mathrm{v}} - \mathbf{P}_{\mathrm{r}}]\} \times 100. \tag{31}$$

   The function abs calculates the absolute value of each component of the difference between $\mathbf{P}_{\mathrm{r}}$ and $\mathbf{P}_{\mathrm{v}}$, and $\Delta P_{\max}$ is the difference between the overall absolute maximum, and the overall absolute minimum of $\mathbf{P}_{\mathrm{r}}$ and $\mathbf{P}_{\mathrm{v}}$.

In Table VII, the force profile, $\mathbf{F}_{\mathrm{r}}$, is found for each of the cases of Table VI. In Figures 19–21, the phase-lead distributions $\mathbf{P}_{\mathrm{r}}$ and $\mathbf{P}_{\mathrm{v}}$ are shown for each case of Table VI. Finally, in Table VIII, the percentage error for each case is calculated by using Eq. (31).

As can be observed from Figure 2, the best fit (minimum percentage error) corresponds to case 6.

5. CONCLUSIONS

In this paper, a photoelastic tactile transducer has been studied by CFEs and FEA to determine the stress distribution, and the theory of photoelasticity has been used for the calculation of the phase-lead distribution. The FEA technique allows one to take into account the effect of the boundary conditions on the phase-lead distribution of the transducer, creating, as a consequence, a more reliable model for the transducer.

[b] Solving Eq. (28) is not trivial! In ref. 20, a neural network was proposed to solve a similar inverse problem. Other solutions to the problem are addressed in refs. 21 and 22.

Table VII. Recovered force profile $\mathbf{F}_r$ for the eight cases of Table V

Case no.	F_1	F_2	F_3	F_4	F_5	F_6	F_7	F_8	F_9	F_{10}	F_{11}
1	0.2469	0.0745	0.05011	0	0	0	0	0	0	0.1258	0.2336
3	0.2359	0.0835	0.0679	0	0	0	0	0	0	0	0
6	0.0999	0.0572	0.01008	0.0715	0.2105	0.2998	0.1186	0.1298	0.1503	0.1098	0.0899

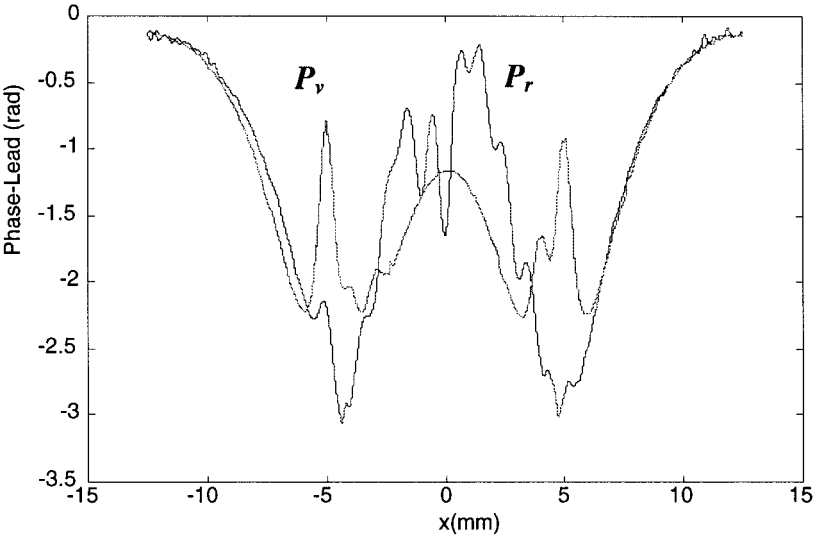

Figure 19. Phase-lead distributions $\mathbf{P}_r$ and $\mathbf{P}_v$ for case 1.

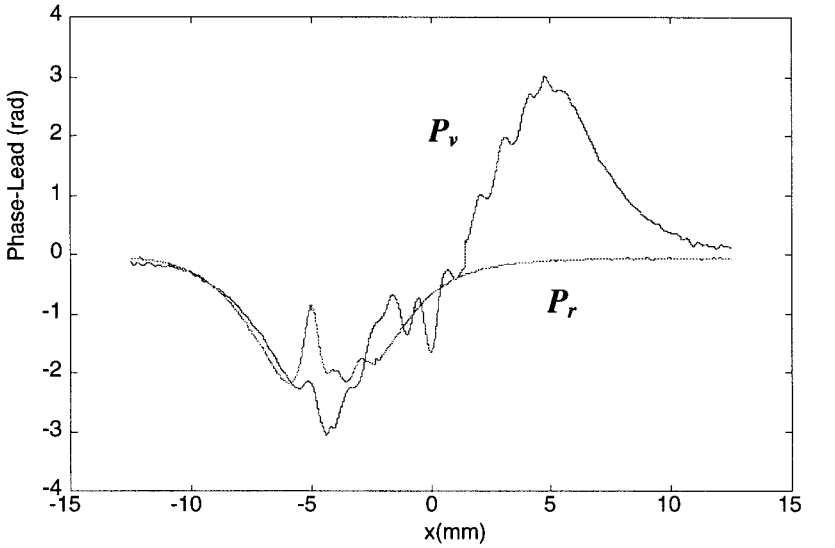

Figure 20. Phase-lead distributions $\mathbf{P}_r$ and $\mathbf{P}_v$ for case 3.

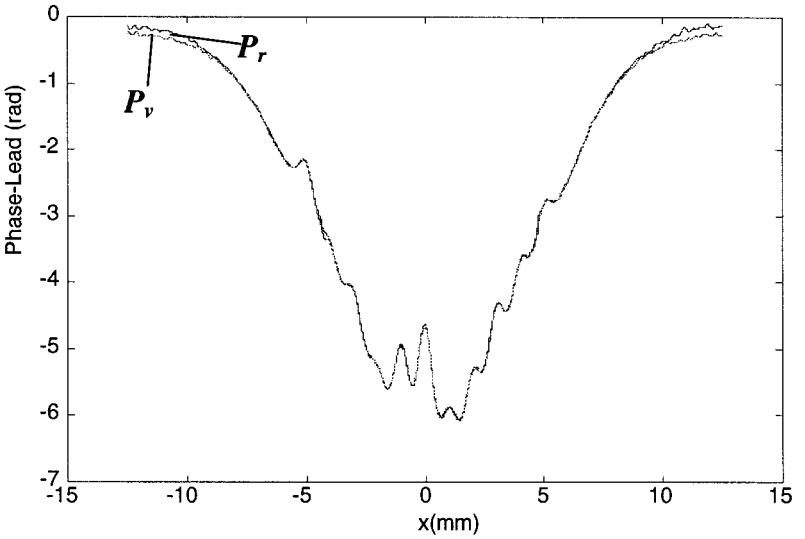

Figure 21. Phase-lead distributions $\mathbf{P}_r$ and $\mathbf{P}_v$ for case 6.

Table VIII. Percentage error for the cases shown in Table V

Case no.	1	3	6
Error (%)	41.4	51.4	3.6

The recovery of the phase-lead distribution from an ideal (noise-free) light intensity distribution has been presented and used to promote an understanding of the ill-posed conditions that may be found when the phase-lead distribution must be recovered from a noisy light intensity distribution. For the latter case, a general algorithm has been presented for the automatic recovery of the phase-lead distribution. In this process, the noisy light intensity distribution is assumed to be detected by a CCD array camera linked to an A/D converter. The algorithm tackles the ill-posed condition of the problem by reducing the set of possible phase-lead distributions and by checking physical properties of the solution. Some simulation results from a 2-D optomechanical finite-element model of the transducer have been presented to demonstrate the proposed algorithm. To solve the inverse tactile problem, an optimization function was successfully implemented.

In practice, finding the correct phase-lead distribution might be computationally time-consuming if each distribution is considered sequentially. This is a consequence of the complexity of the algorithm by which the inverse tactile problem must be solved. However, it is quite possible to process the different phase-lead distributions in a parallel manner: use of dedicated hardware to solve the inverse tactile problem, such as the scheme proposed in ref. 20, for instance, is particularly attractive.

Photoelastic tactile sensors could be implemented in the near future that use integrated optics and optoelectronics, in a manner analogous to piezoresistive tactile transducers that currently use micromachining and microelectronics.[23]

REFERENCES

1. M. M. Frotch, *Photoelasticity*, Vol. 1, John Wiley & Sons, New York, 1960.
2. M. M. Frotch, *Photoelasticity*, Vol. 2, John Wiley & Sons, New York, 1960.
3. P. S. Theocaris and E. E. Gdoutos, *Matrix Theory of Photoelasticity*, Springer-Verlag, Berlin, 1979.
4. H. Aben, *Integrated Photoelasticity*, McGraw-Hill, New York, 1979.
5. S. C. Jacobsen, J. E. Wood, D. F. Knutti, and B. Biggers, ''The Utah/MIT dexterous hand: work in progress,'' in *Robotics Research: The First International Symposium*, M. Brady and R. Paul, Eds. MIT Press, Cambridge, MA, 1983, pp. 601–653.
6. A. Cameron, R. Daniel, and H. Durrant-Whyte, ''Touch and motion,'' IEEE International Conference on Robotics and Automation, Philadelphia, 1988, pp. 1062–1067.

7. K. W. Loh, H. Durrant-Whyte, and R. Daniel, ''A photoelastic tactile sensor,'' Technical Report OUEL 1792/89, Department of Engineering Science, University of Oxford, Parks Road, Oxford, 1989.
8. A. Cameron, R. Daniel, and H. Durrant-Whyte, ''Tactile geometry for images and normal,'' in *Tactile Sensing and the Photoelastic Tactile Sensor*, Technical Report OUEL 1758/89, Department of Engineering Science, University of Oxford, Parks Road, Oxford, 1989, pp. 1–16.
9. F. Eghtedari and C. Morgan, ''A novel tactile sensor for robot applications,'' *Robotica*, **7**, 289–295, 1989.
10. S. H. Hopkins, F. Eghtedari and D. T. Pham, ''Algorithms for processing data from a photoelastic slip sensor,'' *Mechatronics*, **2**, 15–28, 1992.
11. F. Eghtedari, S. H. Hopkins, and D. T. Pham, ''Model of a slip sensor,'' *J. Eng. Manuf.*, **207**, 55–64, 1993.
12. N. Fürstenau, ''Investigation in a tactile sensor based on fiber-optic interferometric strain gauges,'' *SPIE Fiber Optic and Laser Sensor VII*, Boston, MA, Vol. 1169, 1989, pp. 531–539.
13. N. Fürstenau, ''Double-polarization interferometer for digital displacement and force sensing by fiber tension-bending,'' *International Conference on Optical Fiber Sensors*, Vol. 2, Part 1, New Orleans, 1988, pp. 191–194.
14. R. S. Fearing, ''Planar elasticity for tactile sensing,'' in *Advanced Tactile Sensing for Robotics*, H. R. Nicholls, Ed. World Scientific, Singapore, 1992, pp. 75–93.
15. R. S. Fearing and T. O. Binford, ''Using a cylindrical tactile sensor for determining curvature,'' *IEEE Trans. Robot. Automat.*, **7**, 806–817, 1991.
16. R. E. Saad, ''Development of a photoelastic tactile transducer,'' Ph.D. Thesis, Department of Electrical and Computer Engineering, University of Toronto, Canada, 1996.
17. R. E. Saad, A. Bonen, K. C. Smith, and B. Benhabib, ''Distributed-force recovery for a planar photoelastic tactile sensor,'' *IEEE Instrumentation and Measurement Technology Conference (IMTC/95)*, Waltham, MA, April 1995, pp. 532–537.
18. R. E. Saad, A. Bonen, K. C. Smith, and B. Benhabib, ''Finite-element analysis for photoelastic tactile sensors,'' *International Conference on Industrial Electronics, Control and Instrumentation (IECON'95)*, Orlando, November 1995, pp. 1202–1207.
19. K. L. Johnson, *Contact Mechanics*, Cambridge University Press, Cambridge, England, 1985.
20. Y. C. Pati, P. S. Krishnaprasad, and M. C. Peckerar, ''An analog neural network solution to the inverse problem of 'early taction,''' *IEEE Trans. Robot. Automat.*, **8**, 196–212, 1992.
21. W. Nowlin, ''Experimental results on Bayesian algorithms for interpreting compliant tactile sensing data,'' *IEEE International Conference on Robotics and Automation*, Sacramento, CA, 1991, pp. 378–383.
22. J. Z. Sasiadele and P. J. Wojcik, ''Tactile sensor signal processing using an adaptive Kalman filter,'' *IEEE Trans. Robot. Automat.*, Raleigh, NC, 1987, pp. 1753–1759.
23. S. Sugiyama, K. Kawahata, H. Funabashi, M. Takigawa, and I. Igarashi, ''A 32×32 (1k-element silicon pressure-sensor array with CMOS processing circuits,'' *Electron. Commun. Jpn.*, **75**, 64–76, 1992.